
Article:
Fletcher, D.I. orcid.org/0000-0002-1562-4655, Corteen, J. and Wilby, A. (2024) Rough surface rolling contact fatigue crack stress intensity factor calculation for modern rail steels. Wear, 540-541. 205231. ISSN 0043-1648

https://doi.org/10.1016/j.wear.2023.205231

Wear 540-541 (2024) 205231

Contents lists available at ScienceDirect

Wear

journal homepage: www.elsevier.com/locate/wear

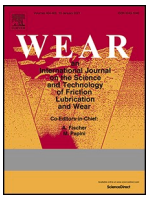

Rough surface rolling contact fatigue crack stress intensity factor calculation for modern rail steels

D.I. Fletcher [a,*], J. Corteen [b], A. Wilby [a]

[a] Department of Mechanical Engineering, University of Sheffield, Mappin Street, S1 3JD, UK
[b] British Steel Research and Development Centre, 7A Seldon Way, Catcliffe, S60 5XA, UK

ARTICLE INFO

Keywords:
Rail
Wheel
Contact
Grinding
Roughness
Fracture mechanics

ABSTRACT

For premium grades (and rail surface treatments such as 'laser cladding') there is little plastic damage expected during typical operating conditions, and smooth surface contact models predict a long life. However, damage still develops, including rolling contact fatigue, affecting premium steels from multiple suppliers. A model is described predicting stress intensity factors and indicative crack growth rates for cracks driven by surface roughness stresses. Accompanying field data quantify the asperity separation and tip radii for rails from metro, mixed traffic and a freight line in ground or unground conditions. The results predict that in rough surface contact small surface cracks (50–100 μm, exceeding microstructural dimensions) can grow faster than crack removal by wear, even when smooth surface models predict no growth. The model has application in identifying how rail grinding marks or wheel roughness may be an important factor in determining rail life through raised stresses at the rail surface (leading to wear), and increased stress intensities and growth rates for incipient cracks.

1. Introduction

Rolling contact fatigue (RCF) cracks in railway rails continue to be a failure mode in rails deployed worldwide. The first understanding of their growth mechanisms was developed in the 1930s and more recent improvement in their understanding has assisted in controlling the problem through methods including rail surface grinding [1], use of harder rail steels [2–4], friction management at the rail-wheel interface [5,6], and better programming of rail inspection [7,8]. Unmanaged rail cracks can be a serious safety issue but while their management reduces safety risks it is also an ongoing cost in running a rail network.

This paper explores a particular case of crack growth in "premium" rail steels (with increased hardness and material strength) that are subject to rough surface contact. This may be due to wheel roughness (e.g. post turning) or rail roughness from rail grinding (Fig. 1). While harder steels aim to slow or prevent RCF initiation it has been observed that cracks still occur in steels from multiple suppliers [9–12]. To guard against this it is therefore reasonable that grinding is deployed to reprofile the rails, redistribute stress and remove any damaged surface material. However, the modelling presented here highlights a sensitivity of crack growth to surface roughness for harder steels in which plastic flow and wear is reduced, and where grinding marks remain on the contact surface for longer than with softer rail steels conventionally used in European passenger rail operations.

The model developed combines established approaches to modelling rough contacts and to calculating stress intensity factors to describe the growth of incipient defects. Considerable research in the rail-wheel contact field has been put into modelling plastic damage [13–15] but here advantage is taken of the minimal plastic flow that is found in modern premium rail steels to simplify the modelling task. Although the material may undergo some very near surface plastic damage this is not usually an ongoing accumulation of strain, it is self-limited as strain hardening and shakedown [16] allow it to reach a quasi-elastic state. Without significant or ongoing plastic flow present there can be much greater confidence in applying elastic contact solutions. Moreover, when looking at surface roughness due to rail grinding this has a distinct surface form which is more easily described than truly random rough surfaces. While fractal based models offer advantages for more complex surfaces [17,18] here an approach using a multi-Hertzian contact developed specifically for ground surfaces is applied [19]. Conversion of the surface pressure distribution from the contact model is undertaken using the crack line Green's functions originally developed by Rooke et al. [20] and previously integrated into rolling contact fatigue fracture mechanics models for smooth surface contact [21–24]. The result is a

* Corresponding author.
E-mail address: D.I.Fletcher@Sheffield.ac.uk (D.I. Fletcher).

https://doi.org/10.1016/j.wear.2023.205231
Received 27 February 2023; Received in revised form 9 November 2023; Accepted 27 December 2023
Available online 6 January 2024

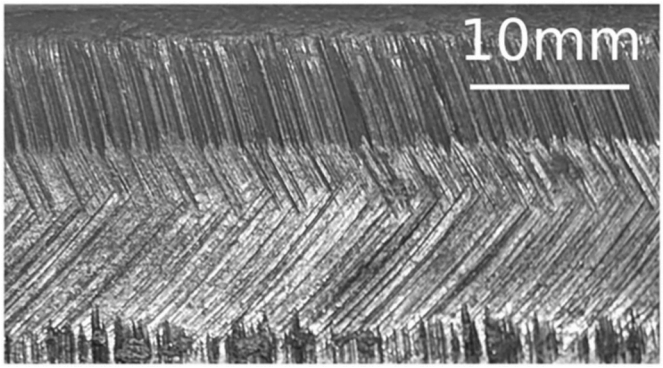

Fig. 1. Rail head surface after in-situ industrial rail grinding.

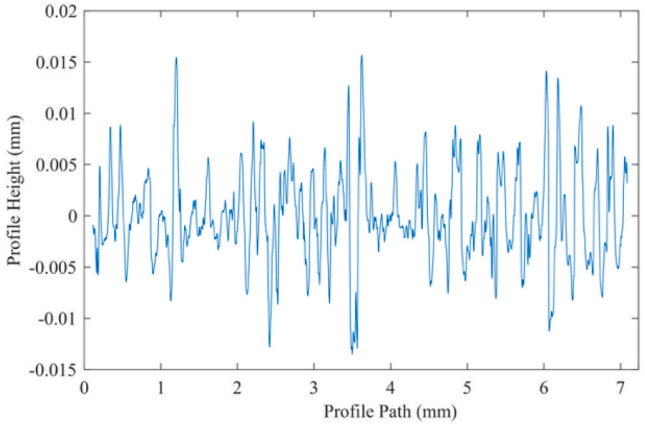

Fig. 2. Surface profile from recently ground premium rail. Note unequal scales exaggerate surface gradients.

fast running model through which parameters relevant to grinding operation can be analysed (i.e. grinding mark sharpness and separation, these being determined by stone composition, stone and vehicle speed during grinding). The aim is to develop a model to explore how grinding may be applied to harder premium steels to safeguard against the rough ground surface itself becoming a driver of rail failure.

To set the context for the modelling, data were gathered on previous measurements of contact surface roughness in rolling contact testing, and also on rail grinding materials from which estimates can be made of ground rail roughness. Additional data are also collected from the field and presented in Section 3 to aid discussion of the stress intensity factor results. In the laboratory wear testing of rail steels under water lubricated conditions Kapoor et al. [25] identified asperity tip radii around 130 μm, falling to 92 μm after testing. Pre-test asperity separation (i.e. wavelength) was 20 μm, falling to 12 μm after testing. Recent work by the authors on dry wear lab testing of 260 grade rail steels has identified pre-test asperity tip radii in the order of 200 μm and separation of 55 μm, rising marginally to around 250 μm tip radius and 70 μm separation after testing. Focusing on much harder steels Clarke et al. [26] conducting mineral oil lubricated tests on 800-840Hv surface hardness gear steel observing asperity tip radii in the order of 16 μm prior to testing and 75–80 μm after testing. Zhang et al. [27] developed rail grinding wheels using grit sizes of F10, F16 and F30, which convert to sizes of 600, 1180 and 2000 μm. Although the grinding marks left will depend on the action of multiple non-aligned grit particles and the stone traversal speed it's clear that surfaces produced could never approach the smooth surfaces typical of most laboratory tests. Fig. 1 shows a typical rail surface after industrial in-situ grinding with around 25 prominent grinding marks per 10 mm length, i.e. an asperity separation of around 400 μm. On the wheel side of the contact interface data from Lundmark [28] shows that post turning train wheels have a surface wavelength in the 1–2 mm range, with peak to trough variation in surface height of 30–100 μm depending on the wheel material and how aggressive the turning operation was. How long this severe level of roughness persists will depend on the wheel materials and operating conditions, and as for rails there are clearly many variables. However, the aim here is not to choose specific values for modelling but to ensure that the model developed considers values in the right range. Fig. 2 shows a typical roughness trace from a recently ground rail to further support estimation of the roughness characteristic of industrial rail grinding.

2. Contact model and stress intensity factor calculation

2.1. Contact model

The contact model is fully described by Nowell and Hills [19] and only a summary is present here. The model idealises the contact pair as a perfectly smooth 2D wheel in contact with a rough rail (realistically both surfaces will be rough, especially if wheels have recently been turned, but numerically the combined roughness can be represented in this form). Asperity contacts (i.e. at peaks in ground surface form) are represented by an asperity tip radius (ρ) and wavelength (λ) as shown in Fig. 3. The number of asperities in contact is estimated initially from the smooth surface Hertzian contact patch size, and applied load divided to establish initial values of pressure and contact size at each asperity. Surface deformation due to each asperity will affect its neighbours and an iterative procedure is followed to achieve compatibility of load distribution and surface deformation across the contact. Key factors in application of this model for harder rail steels are (i) surface form and grinding marks persist because of high yield strength and very limited plastic flow, and (ii) the high yield point makes use of an elastic model a reasonable assumption.

Once convergence is achieved there is a known list of asperity loads (and hence contact sizes and pressures) representing the rough surface contact. These transmit the same total surface load as the corresponding smooth surface Hertzian contact. With the array of asperity loads and sizes on the contact surface established the interior sub-surface stresses can be calculated by superposition of standard Hertzian stress calculations [29] applied to each asperity.

2.2. Stress intensity factor calculation

Green's functions are a means to capture the results of a stress intensity factor calculation and apply them to a range of load cases. Functions developed by Rooke et al. [20] convert a point force on the line of an inclined surface breaking crack onto a stress intensity factor for that crack. By integration any arbitrary load distributed along the crack line can be treated as a summation of point forces for calculation of the combined stress intensity factor for the total applied load. Both normal and shear loads along the line of the crack can be considered providing calculation of mode I and II stress intensity factors. In all cases the method uses the stresses present in the uncracked body to calculate the stress intensity factors, agreement with Bueckner's principle [30].

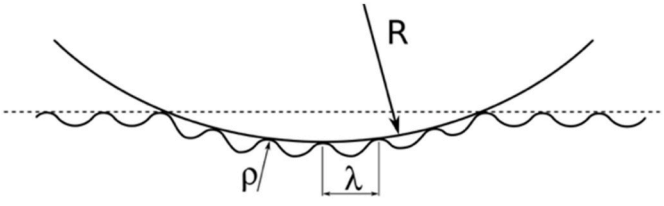

Fig. 3. Multi-Hertzian contact between a smooth wheel and ground surface represented by grinding mark wavelength λ, and surface peaks of radius ρ. Equivalent radius for the contact pair is R. After [19].

Equations (1) and (2) summarise the process for a normal (σ) and shear (τ) stress distributions along a crack line of length *s*. The axis along the crack direction is *η*, and θ is the crack angle defined in Fig. 4. Separate Green's functions (*g*) are used for normal and shear stress contributions to K_I and K_{II} at the crack tip. The stress present on the crack line is also dependent on the offset (*e*) between the origin at the crack mouth and the centre of the contact patch.

$$K_I = \frac{1}{\sqrt{\pi s}}\left(\int_0^s \sigma(\eta,\theta,e)g_{\sigma_I}(\eta)d\eta + \int_0^s \tau(\eta,\theta,e)g_{\tau_I}(\eta)d\eta\right) \quad (1)$$

$$K_{II} = \frac{1}{\sqrt{\pi s}}\left(\int_0^s \sigma(\eta,\theta,e)g_{\sigma_{II}}(\eta)d\eta + \int_0^s \tau(\eta,\theta,e)g_{\tau_{II}}(\eta)d\eta\right) \quad (2)$$

A complication with rolling contact fatigue cracks is that they are frequently loaded in compression and account must be taken of crack face interaction and crack face friction forces (τ_{cff}) which will act to oppose sliding of the crack faces. As in previous models [21,23] the assumption is made that where crack faces meet, the normal stress contribution to crack opening is set to zero (the crack cannot be more than closed). Where crack faces meet the normal load multiplied by a crack face friction coefficient (μ_{crack}) must be overcome to produce crack face shear. The stress within the body from the multi-Hertzian solution (σ_{nom}, τ_{nom}) is therefore modified according to Equations (3)–(5).

$$\sigma(\eta,\theta,e) = \max[\sigma_{nom}(\eta,\theta,e), 0] \quad (3)$$

$$\tau_{cff}(\eta,\theta,e) = -\mu_{crack} \bullet \sigma_{nom}(\eta,\theta,e) \bullet sgn(\tau_{nom}(\eta,\theta,e)) \quad (4)$$

$$\tau(\eta,\theta,e) = \begin{cases} 0 \\ \tau_{nom}(\eta,\theta,e) + \tau_{cff}(\eta,\theta,e) \\ \tau_{nom}(\eta,\theta,e) \end{cases} \quad (5)$$

$$\begin{array}{c} \text{if } |\tau_{nom}(\eta,\theta,e)| \le |\tau_{cff}(\eta,\theta,e)| \text{ and } \sigma_{nom}(\eta,\theta,e) < 0 \\ \text{if } |\tau_{nom}(\eta,\theta,e)| > |\tau_{cff}(\eta,\theta,e)| \text{ and } \sigma_{nom}(\eta,\theta,e) < 0 \\ \text{if } \sigma_{nom}(\eta,\theta,e) \ge 0 \end{array}$$

The crack growth mechanism is assumed to be primarily by shear crack growth and fluid is considered only as a crack face lubricant, not as a fluid pressurising the crack. This follows previous investigation [31] which explored the three-dimensional nature of typical RCF cracks showing the complete sealing and pressurisation of fluid in the cracks is unlikely, and that if such fluid pressurisation was achieved the predicted growth rates become unrealistically high. The modelling concept is shown schematically in Fig. 4 where the previous approach (part a) is replaced by the multi-Hertzian approach (part b). To obtain the full range of stress intensity factor variation during the passage of a contact over the crack the analysis must be performed at increments of contact

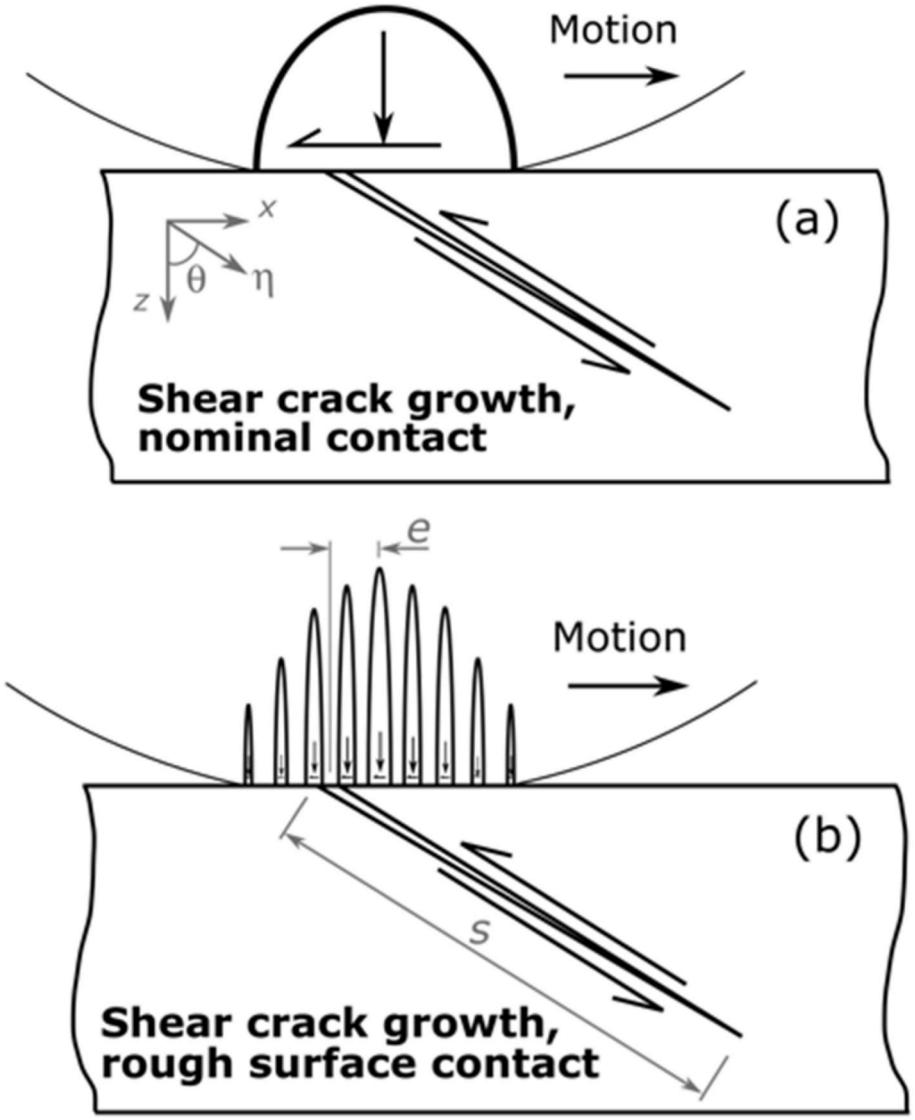

Fig. 4. Modelling concept and axis definitions: (a) nominal smooth Hertzian contact, (b) replacement by a multi-Hertzian representation of a ground surface contact.

movement relative to the crack. For smooth surface contact a typical contact movement increment of 0.05 times the contact half width (a) is fully sufficient to capture peaks in stress intensity factor as the contact passes the crack. For the rough surface contact much finer movement increments are needed to capture the highly localised stress fields from the asperities, especially when studying near surface cracks. A factor of $0.001a$ was used for near surface cracks with relaxation to $0.01a$ being sufficient for longer cracks for which the tip is more distant from the localised stress peaks. The longitudinal region explored covered the range $e = \pm 15a$.

In making the transition to a rough surface contact it's crucial to note that superposition of stress on the crack from all the asperities must always be considered ahead of integration of the resultant stress with the Green's function to find the stress intensity factor. Calculation of the stress intensity factors from individual asperities followed by superposition of the stress intensity factors would fail to correctly capture the crack opening and sliding behaviour which is dependent on the superposed stress. Taking the crack mouth as the origin, examples of the crack

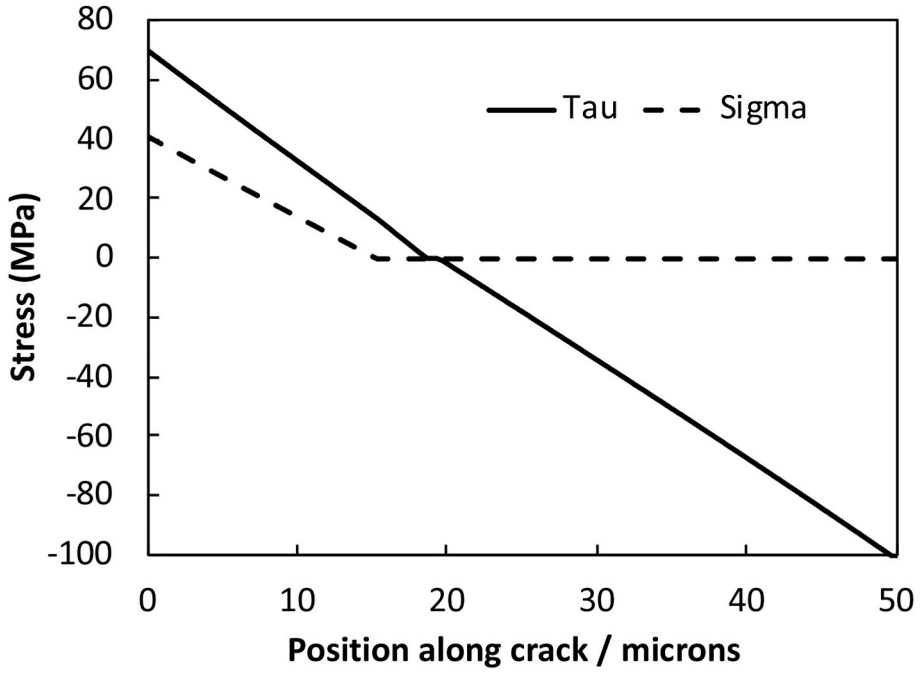

(a)

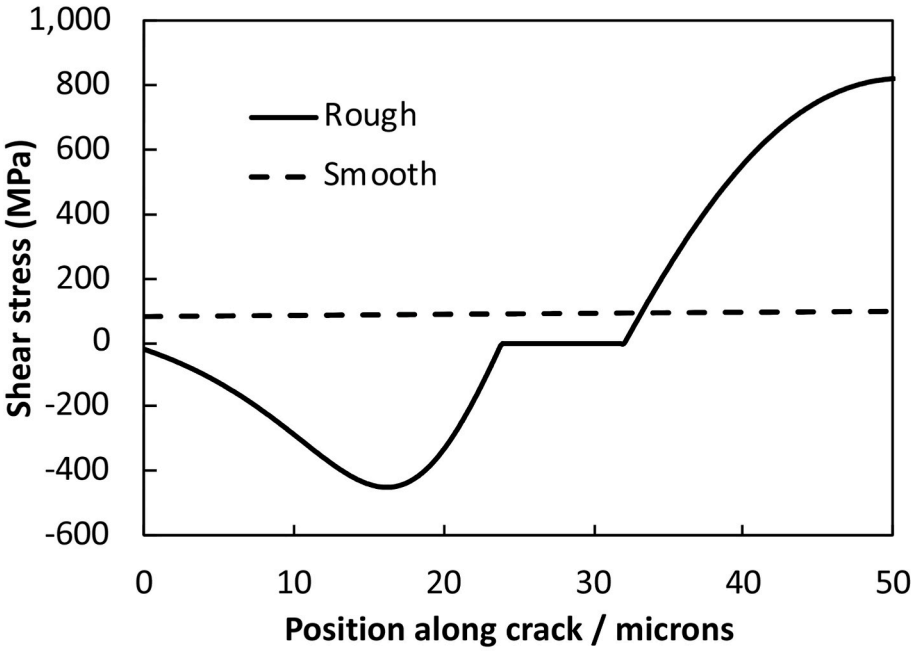

(b)

Fig. 5. Stress distributions from Equations (3) and (5) along the line of a 50 μm crack 30° below a full-size rail-wheel contact of nominal contact pressure 900 MPa. Roughness wavelength 0.4 mm, asperity tip radius 0.25 mm. The position origin is the crack mouth. (a) Normal (sigma) and shear (tau) stress for rough surface contact resolved along the line of the crack. Contact is at position e = −2.96 mm (0.49a to the left of the crack mouth in Fig. 4). (b) Comparison of shear stress for rough and smooth contact models. Contact at e = −5.96 mm (0.98a left of the crack mouth).

line stresses from Equations (3) and (5) are shown in Fig. 5 for both the smooth and rough surface models at identical contact positions. Fig. 5a indicates that for the position modelled the normal stress is zero at the crack tip, but that the crack is open closer to the rail surface. The shear stress changes sign part way along the crack with a short region of zero stress indicating a locked region of the crack which makes no contribution to crack growth. These values are for the rough surface contact whereas the corresponding data for a smooth contact are zero throughout (crack closed, no crack sliding). Fig. 5b compares rough and smooth solutions directly, considering only the resolved shear stress driving crack growth only (the crack was closed throughout so sigma values were all zero for both cases). Smooth contact has a low constant (non-zero) resolved shear stress driving crack growth. The rough surface model shows higher values, and a switch from negative to positive shear with movement along the crack line, i.e. with movement through the stress field. The zero region at the mid crack location for the rough surface contact is the location of reversal in shear stress sign. This region is locked (i.e. the applied stress cannot overcome crack face friction) so there is no contribution to driving crack growth in this region.

3. Results

3.1. Modelling runs undertaken at full scale

Table 1 summarises the parameters used in the modelling. These are used to describe a manufactured surface (ground rail or turned wheel), so can include some combinations that would be unlikely in naturally worn surfaces. For example, widely spaced asperities of tip radius much smaller than their separation would be unlikely to occur naturally, but can be generated by grinding or turning operations. Although it would be possible to nondimensionalise the analysis the ground surface parameters (surface wavelength and asperity tip radius) are lengths that do not scale with the contact size so a dimensional approach was taken. The friction coefficients chosen are representative of water lubricated rail-wheel contact during which fluid assisted crack growth becomes possible, and are applicable across metro, mixed traffic, and freight railways. Modelling for dry contact conditions (friction coefficient 0.4) was also undertaken but extensive contact fatigue cracking does not develop under these conditions so results for this case are restricted to some comments in Section 3.3.2.

Results are presented first of stress on the rail cross-section below the contact. This provides context on the depth of rail material affected by roughness stress and confirmation that the aggregate effect of the multiple asperity contacts is equivalent to the smooth surface case supporting the same load. Further results are in terms of stress intensity factors for growth of an inclined surface breaking crack at 30° below the contact surface, corresponding to a typical rolling contact fatigue crack orientation. The method is equally applicable to steeper or vertical cracks using alternative Green's functions which are available for angle θ to the surface normal of 0, 5, 10, 15, 30, 45, 50, 55, 60° [20].

Table 1
Parameters used for modelling runs.

Parameter	Values
Nominal smooth surface contact pressure, MPa	900, 1500
Surface coefficient of friction	0.15
Internal crack face friction coefficient	0.15
Wheel radius, mm	390
Contact loads, N/mm	8601.1, 23892.0
Nominal smooth surface contact half width (a)/ mm	6.08, 10.14
Crack sizes	0.001a to 5a
Crack angle	30° below the surface ($\theta = 60°$)
Asperity tip radius (ρ), microns	50, 150, 250, 350, 550, 750
Asperity separation/wavelength (λ), microns	100, 200, 400, 600
Young's modulus, GPa	210
Poisson's ratio (plane strain model)	0.3

Calculation of stress intensity factors requires that a crack exists, but no attempt is made to model the initiation of the cracks here. This initiation is usually ascribed to plastic ratcheting and ductility exhaustion, and although harder steels usually display very little plastic damage the raised stress caused by the rough surface may drive this very locally to the contact surface. Early stage plastic damage and the extension of its experimental investigation to include the effect of roughness is the subject of a separate paper [32].

While the main focus of the results is on mode II stress intensity factors which are especially significant for shear mode crack growth it is also useful to convert these to a crack growth rate. A mixed mode crack growth law was developed by Bold and Brown et al. [33,34] and this is applied with the caveat that it was developed for older normal grade rail steel. Its output is therefore only indicative of how the crack will respond to the applied stresses. For a more comprehensive assessment of crack growth the wear of the rail surface which takes place with passing contacts should also be considered and this is discussed alongside the crack growth data. Equation (6) shows the crack growth law used to predict crack tip advance rate. Stress intensity factor ranges are in MPa. $m^{0.5}$ and crack growth rate is predicted in nm/cycle. The equivalent stress intensity factor range ΔK_{eq} is defined in Equation (7) and used to combine the mode I and II factors. Net crack growth (crack tip advance minus cut back of the crack mouth by wear) can be estimated from the results plots through a shift of the vertical axis. Equation (6) contains a threshold stress intensity ΔK_{th} below which no crack growth would be predicted for which a value of 4 MPa $m^{0.5}$ was used [34].

$$\frac{ds}{dN} = 0.000507\left(\Delta K_{eq}^{3.74} - \Delta K_{th}^{3.74}\right) \tag{6}$$

$$\Delta K_{eq} = \sqrt{\Delta K_I^2 + \left[\left(\frac{614}{507}\right)\Delta K_{II}^{3.21}\right]^{2/3.74}} \tag{7}$$

Rooke's Green's functions were developed for a crack of infinite width (corresponding to a 2D contact system) but in the current work a geometry factor of 0.59 [22,23] is applied prior to crack growth rate calculation to convert the stress intensity factors to those for a semi-circular crack more representative of the cracks found in a rail.

3.2. Stress data

Fig. 6 shows data on sub-surface shear stress in example cases of smooth and rough surface contact. In combination with the vertical and longitudinal direct stress this is the primary driver of mode II shear crack growth. It can be seen that the rough surface contact in Fig. 6a has the aggregate effect producing stress identical to the smooth surface model (Fig. 6b) once below around 1 mm from the rail surface. Fig. 6c shows the detail of some of the rough surface contacts illustrating that each is represented by its own micro-contact of similar stress distribution but higher pressure than the macro contact.

While plots such as these are well established for rough surface contact they illustrate an important issue when approaching crack modelling. For very small near surface cracks (up to 100–200 μm in the current case) the crack will be unaware of the macro contact formed by superposition of the micro contacts, and instead experience distinct stress cycles produced by the individual micro contacts. While the roughness modelled is attached to the rail and therefore stationary relative to a rail crack, it is useful to recall that the roughness represents the combination of wheel and rail roughness. For a real system with a rough wheel and high degree of sliding a near surface rail crack will experience multiple stress cycles as the micro contacts slide past. For a rail coarsely ground a rail surface crack will experience primarily the stress field of prominent asperities (grinding marks) whose asperity stress fields will dominate the local material to produce high peak stresses as a wheel moves past. This will give a roughness driven stress cycle even as a wheel passes without significant slip in the contact. The

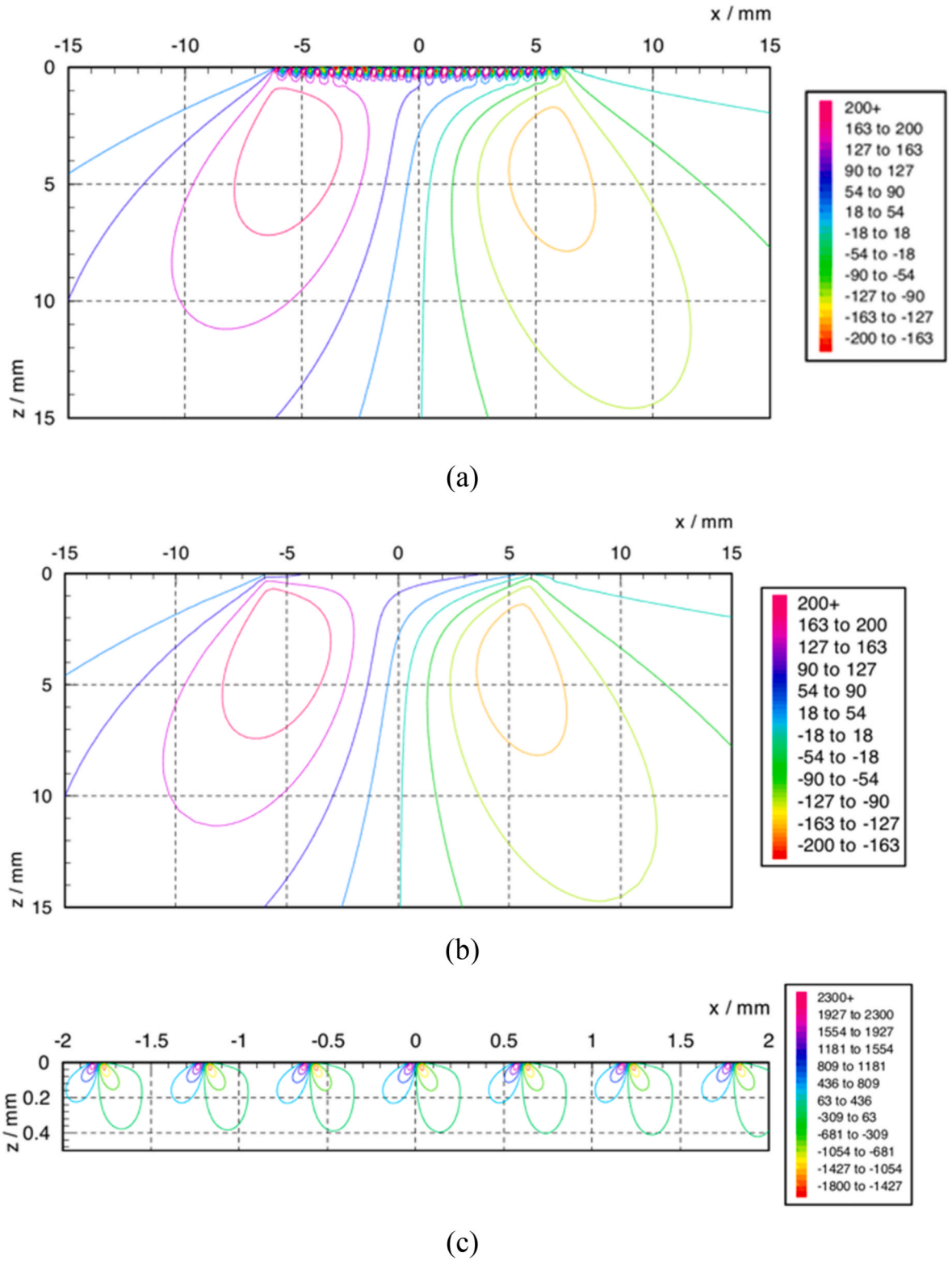

Fig. 6. Orthogonal shear stress (MPa) on a longitudinal cross-section below the rail surface for a nominal smooth surface contact pressure of 900 MPa with a 0.6 mm roughness wavelength of asperities of 0.25 mm tip radius. (a) Rough surface model. (b) Equivalent smooth surface case transmitting the same load. (c) Detail extracted close to the surface of the rough surface case.

analysis could also be reapplied to consider cracks in the wheel surface. As cracks extend the superposition of multiple micro-contacts smooths out the changes in stress and the crack begins to see a single cycle of stress during the macro contact pass. This complexity over the number of stress cycles seen at a particular depth raises a question in converting stress intensity factors to crack growth rates. Near surface cracks will see both high stress intensity factors (not predicted in smooth surface models) and potentially multiple stress cycles, producing a particularly damaging combination.

3.3. Stress intensity factors

3.3.1. Variation of position within the contact patch

Prior to considering the change of stress intensity factor with crack length it is useful to look at the detail of how stress intensity factor varies with contact position (*e*) relative to the crack. Considering a crack with its mouth at the origin (as in Fig. 4b) Fig. 7 shows the stress intensity cycle produced as a contact patch approaches the crack, moving over it and moving away. As discussed above the combined wheel and rail roughness modelled is mapped to the rail surface and so is necessarily stationary relative to the crack. However, in the real contact there will be an element stationary relative to the crack (rail roughness), and an element which could also slide relative to the crack (wheel roughness). For a 50 μm long crack there is very high sensitivity to the roughness either through potential to be exposed to a very high individual peak in stress intensity (i.e. for a crack growing close to an asperity location on the rail), or to experience a series of high and reversing stress intensity peaks (for the case of a rough wheel passing with rolling-sliding motion). In the case of rail roughness dominating the combined roughness a stress intensity factor range would be defined by transition from stress free (prior to contact arrival) to a positive or negative peak value very close to those that would define this range for the sliding passage of a similarly rough surface wheel. But while a sliding rough contact passage would produce multiple stress cycles there would be only one cycle for a crack stationary relative to the rail roughness.

For a 2 mm long crack the effect of individual asperities is still evident with variation of *e*, but the overall stress intensity cycle is much more significantly dependant on the superposition of all asperities to form a macro contact. For a 6 mm long crack the stress intensity cycle has greater magnitude (the crack is reaching sub-surface peaks of reversing shear stress, Fig. 6a) but still contains a minor ripple which would not be present in a smooth surface solution. Although the crack tips for 2 mm and 6 mm long cases are well away from the localised asperity stresses they are still influenced by them as the crack mouth remains at the surface and subject to individual asperity loads. As described by Equation (1) the crack tip stress intensity factor is dependent on the stress distribution along the full length of the crack.

The results in Fig. 7 are non-symmetrical about the origin as the crack is inclined at 30° below the surface, and shear traction is applied at the surface giving a non-symmetrical system. The results for mode I follow a similar pattern, but are of low magnitude given the compressive nature of the contact.

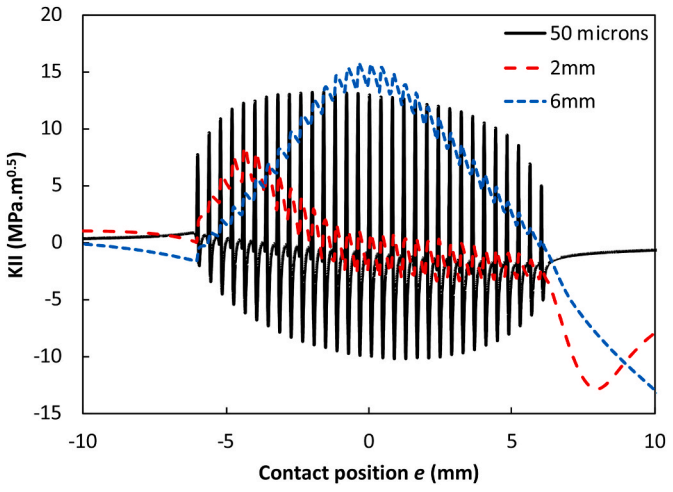

Fig. 7. Predicted variation of mode II stress intensity factor for a range of contact positions (e) for a crack at the origin for crack lengths 50 μm, 2 mm, and 6 mm. Nominal contact pressure 900 MPa, λ = 0.4 mm, ρ = 0.25 mm.

3.3.2. Variation of asperity separation wavelength

Fig. 8a shows results for mode II stress intensity factor range assuming the full passage of the contact over a crack. The data is for a nominal 900 MPa contact and asperity tip radius ρ = 0.25 mm. The smooth surface case is provided as a baseline, indicating that very low stress intensity factors would be present for short cracks, with a high possibility that they would not exceed the threshold stress intensity factor (Equation (6)) and therefore experience no crack tip advance. This is indicated in Fig. 8b for which the smooth surface growth rate is zero until cracks exceed around 0.25 mm in length.

When roughness is introduced a peak in mode II stress intensity factor develops at short crack lengths at which cracks are highly influenced by the near surface stress field. The increase is dependent on the asperity separation (λ), and with other factors held constant the short crack peak in stress intensity factor range during the passage of the contact increases approximately linearly with λ (the same is true if considering just a single peak in stress due to a rail surface roughness stationary relative to the crack during passage of a smooth wheel). The nature of the crack growth law means this maps to a non-linear increase in the predicted crack growth rate (Fig. 8b). This highlights a particular sensitivity to roughness wavelength which may be influenced by grinding stone choices and operation.

To fully assess crack growth the removal of the rail surface by wear (or grinding) and its effect in shortening cracks should be considered to find the net change of crack length. Rail wear rates could be raised by rough surface contact stress peaks but are typically below 1 nm per

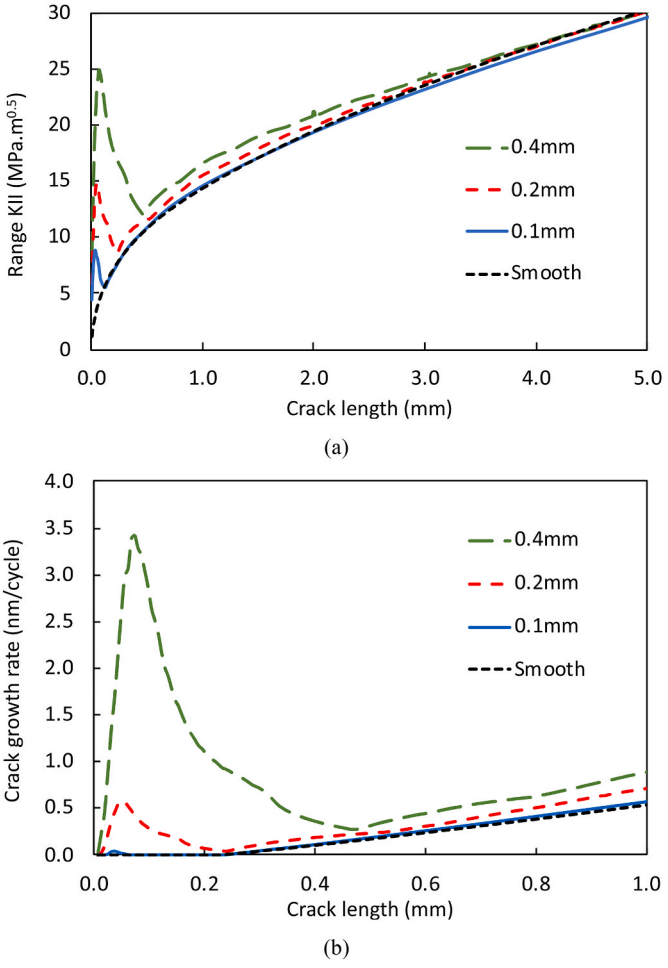

Fig. 8. Effect of asperity separation (wavelength, λ) on (a) mode II stress intensity factor range and (b) indicative crack growth tip advance rates. All cases are nominal 900 MPa contact and asperity tip radius ρ = 0.25 mm.

wheel pass, and from Fig. 8b it can be seen that this rate is comparable with the predicted growth rates. If wear (also taking into account crack inclination) shortens a crack faster than the crack tip advances into the rail then the crack will eventually disappear. From the curves plotted it's clear that a wear rate in the order of 1nm/cycle could exceed the predicted crack tip advance for the smooth surface model at the range of crack lengths plotted. It would therefore be predicted that any small cracks would be safely worn away. However, for the models considering roughness, especially at wider asperity separations, it's unlikely that the developing crack would be removed by wear. The fall back in crack growth rate at around 0.5 mm length may offer a point for cracks to stabilise in a dynamic equilibrium of surface wear and crack tip advance. However, it's unlikely the rail would naturally become crack free by wear if crack growth remains driven by surface roughness.

As crack length extends it can be seen that all the cases modelled tend back towards the smooth surface solution, becoming almost identical by 5 mm length. It's not expected that they become fully identical as the crack mouth of even long cracks remains exposed to the roughness derived near surface stresses. The results in Fig. 8 are for surface and crack face friction coefficients of 0.15, representing water lubricated contact which is a typical condition for contact fatigue crack growth. Modelling for surface and crack face friction coefficients of 0.4, representing dry contact conditions, also showed an increase in stress intensity factor and growth rates at short crack sizes (<300 μm). However, even with this roughness derived increase the near surface values and those for large cracks remained lower than those for water lubrication. While roughness has potential to create shallow surface damage under dry conditions the conventional understanding that extensive crack propagation does not occur in completely dry conditions remains unchanged by its inclusion in the model.

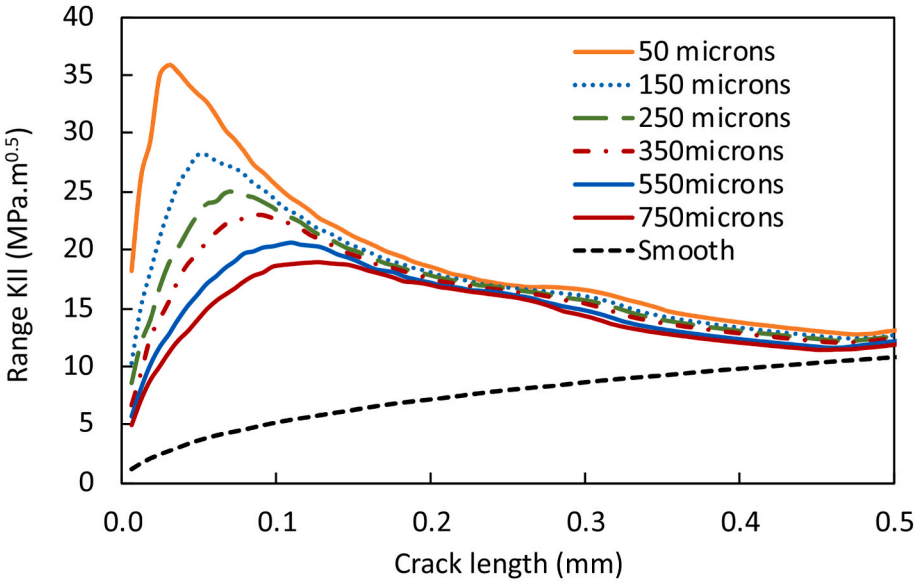

(a)

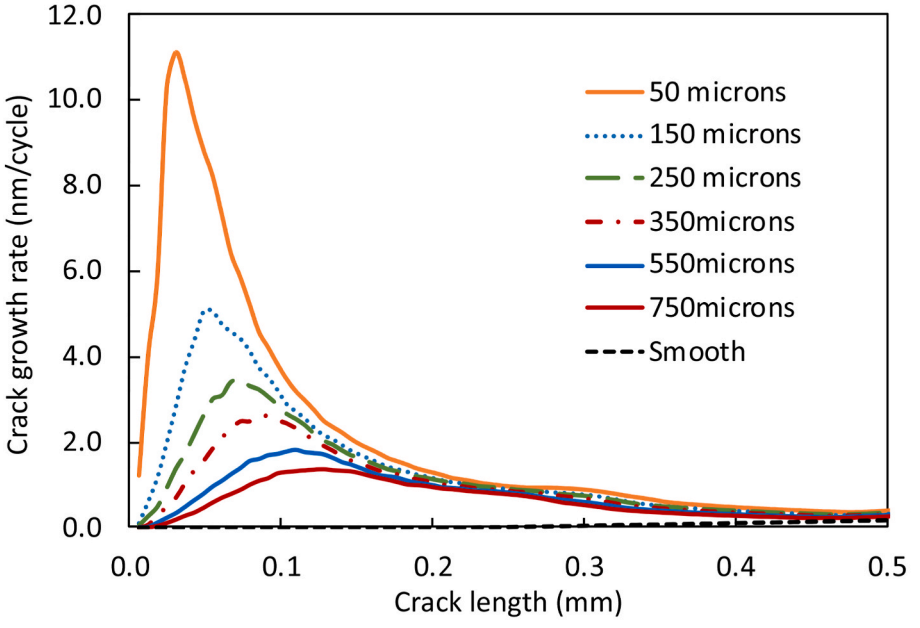

(b)

Fig. 9. Effect of asperity rip radius (ρ) on (a) mode II stress intensity factor range and (b) indicative crack growth tip advance rates. All cases are nominal 900 MPa contact and asperity separation λ = 0.40 mm.

3.3.3. Variation of asperity tip radius

Fig. 9 shows plots of data to explore the effect of asperity tip radius on mode II stress intensity factor range and predicted crack growth rates. The data is for a nominal 900 MPa contact and asperity separation λ of 0.40 mm. It can be seen that sharper smaller radius asperity tips lead to increased stress intensity factor ranges for short cracks. But sensitivity to the asperity tip radius is confined to cracks up to around 0.15 mm long. Beyond this crack length the inclusion of roughness in the model increases stress intensity factor range relative to the smooth surface baseline case, but values are very little affected by the tip radius.

Translating the stress intensity factors to crack tip advance estimates Fig. 9b shows that the smallest radius asperities are predicted to drive rapid advance of short cracks. But for a wide range of larger radius asperities there's much reduced sensitivity of crack advance rates to the exact radius modelled. The tip radius is a difficult quantity to define, even for a manufactured surface, so it is reassuring that the sensitivity of the results to this parameter is low over a wide range of values relevant to industrial grinding.

3.3.4. Effect of nominal contact pressure

Fig. 10 summarises data to show the impact of nominal smooth surface contact pressure on stress intensity factor and estimated crack growth rate. As would be expected for an elastic system the stress intensity factors rise for the higher pressure contact, but the non-linear nature of the crack growth law gives significant increases in the predicted crack tip advance rates. Overall patterns of behaviour are unchanged from the 900 MPa cases explored in the previous sections, but crack advance is significantly more likely to exceed the order of 1 nm typical wear rate with little opportunity for stabilisation at the 0.5 mm crack length 'dip' between roughness driven and bulk behaviour driven crack growth.

3.3.5. Field data on roughness

While some data on surface roughness are available and were briefly summarised in Section 1, these are primarily from laboratory test specimens which are smoother than the ground rail surface shown in Fig. 1. To aid interpretation of the results for field application additional data were collected from two ground and two as-used service rails. These covered metro, mixed traffic passenger/freight and a freight only line, these being selected based on their availability for measurement. The ground rails could not be measured immediately post-grind but profiles were taken from outside the running band to quantify the ground surface unmodified by traffic. An Alicona PortableRF infinite focus microscope with a ×10 objective lens was used to make 3D scans of the rail head surface from which data were extracted with a cut-off length of 250 μm for 2D line profiles orientated parallel to the rail longitudinal direction. Significant asperities were identified as those standing above 30 % of the mean roughness profile peak to valley height (R_z), an adaption of the procedure in BS EN ISO 4287:1998 [35] for identifying significant profile peaks and troughs when measuring the mean separation of profile irregularities (R_{sm}). A circular relationship was fitted to the profile data at each asperity identified, pinned symmetrically at the two nearest mean line crossings, and with maximum height equal to the maximum height of that asperity (see Fig. 11). The asperity separation was determined by the profile length between the centres of each fitted circular relationship. The data generated are summarised in Fig. 12 where it can be seen that for both asperity separation and tip radius the distribution of readings was skewed towards the lower end of the range observed, as indicated by median lines positioned towards the lower end of each box. The medians rather than means therefore gives a more representative single number with which to compare the quantities (Table 2).

From the collected field data it can be seen that the ground rails had significantly reduced asperity tip radii than were found on the naturally worn rails. Cross-referencing this to the results in Fig. 9 indicates that any initiated crack in the ground rail is likely to experience greatly increased mode II stress intensity factors relative to the same crack in a natural condition rail, with much higher indicative crack growth rates. Asperity separation was found to be larger for the ground rails, although there was greater cross-over with the range of separations seen on the naturally worn rails. From Fig. 8 it can be seen that the wider asperity separation is also predicted to lead to higher stress intensity factors (and indicative growth rates) than for the unground rails.

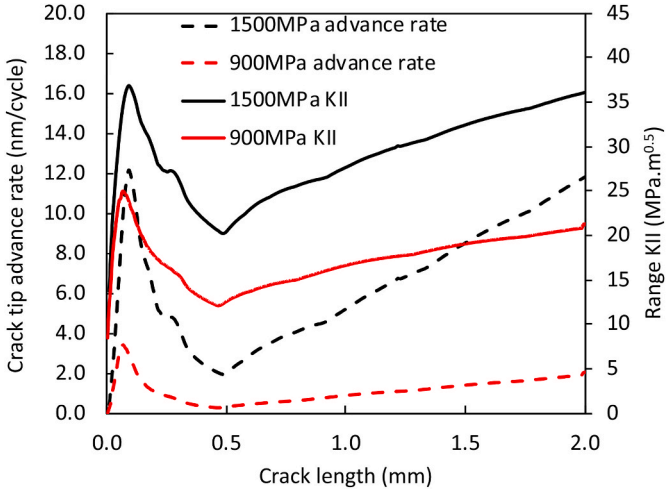

Fig. 10. Effect of nominal contact pressure on mode II stress intensity factor range and crack tip advance rate for 900 and 1500 MPa cases, both for asperity tip radius ρ = 0.25 mm and asperity separation λ = 0.40 mm.

4. Conclusions

A rapid method of assessing stress intensity factors for growth of cracks under rough surface rail-wheel contact has been developed. This combines an established rough surface contact model with a crack line Green's function approach to stress intensity factor calculation. The simple rough surface description used is suited to ground or otherwise manufactured surfaces, using an asperity separation and tip radius to quantify the surface. The combined model is fast and demands little computing power allowing wide exploration of how rough surface parameters affect crack growth predictions. Rail-wheel contact roughness may exist as a result of rail grinding or due to contact with (for example) recently turned wheels. The combined models are particularly suited to application for modern harder "premium" rail steels in which grinding marks can persist over an extended period of time as very little wear or plastic flow is experienced in service (dependent on the type of traffic).

Example cases have been explored for a range of conditions applicable to the rail-wheel case and surfaces characteristic of industrial grinding operations. It is identified that near surface roughness derived stress can raise stress intensity factors for embryonic cracks. This raises

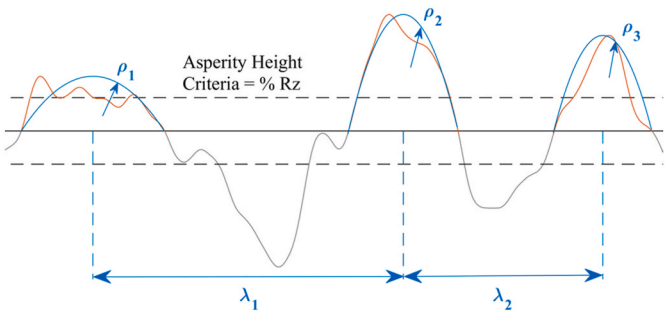

Fig. 11. Schematic representation of determining significant asperity dimensions.

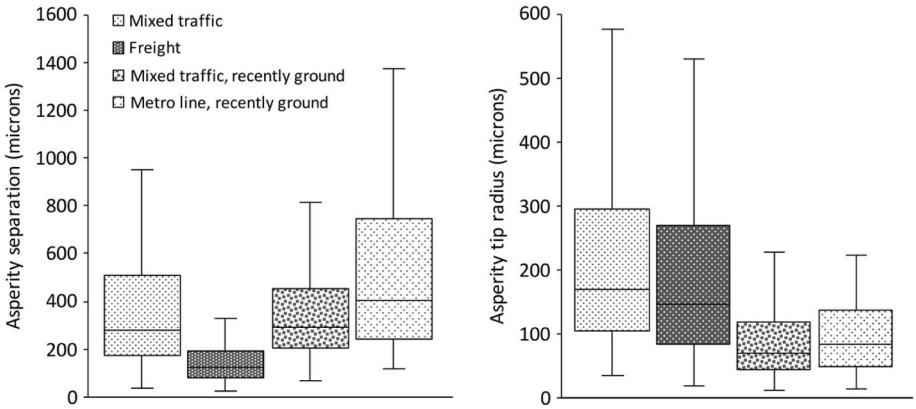

Fig. 12. Surface roughness data from field rails. The central marks are the median, with the box extending to the 25th and 75th percentiles. The whiskers extend to the most extreme data points excluding outliers (considered to exceed the 75th percentile plus 1.5 times the interquartile range and similarly for the lower end of the scale).

Table 2
Median asperity separation and tip radius for field rails, for a mean of 140 asperities measured in each case.

Rail site	Separation (μm)	Tip radius (μm)
Mixed traffic	281	169
Freight	147	127
Mixed traffic, ground	293	71
Metro line, ground	402	83

the potential for even very small cracks (50–100 μm, exceeding microstructural dimensions) to grow in cases where smooth surface models predict sub-threshold stress intensity factors. Growth rates are estimated through an existing crack growth law for rail steels indicating crack tip advance rates comparable and often exceeding typical rail surface wear rates.

Sensitivity of stress intensity factors for a range of crack sizes to the parameters quantifying the surface is explored. It is found that asperity separation has a significant impact on the predictions, whereas asperity tip radius has a highly localised effect which drops away very quickly with distance below the surface.

The model has been developed through consideration of full-size rail wheel contacts, but has the benefit of being equally applicable to laboratory twin disc contact simulations. These typically have a much smaller contact area and there have been persistent questions about scaling between laboratory and real-world cases. Scaling the effects of roughness on contact pressure was previously possible using the contact model alone, but here the comparison can be extended to understanding the effect of scaling on the growth of cracks.

For industrial application the model has particular application in identifying how rail grinding or wheel roughness may drive damage in rails. Newly collected field data shows that ground rails are characterised by reduced asperity tip radii and increased asperity separations relative to unground worn rails. It is now possible to predict how these rough surfaces may drive growth of an embryonic crack, and predict the reduction of growth possible through selection and operation of a finer grade grindstone capable of avoiding damaging widely separated grinding marks on the rail. Consideration of a wider range of operating conditions (particularly different rail friction levels) can be conducted in future to expand understanding of crack transition from roughness to bulk stress driven growth. Extension to the work is possible through superposition of additional stresses to better understand their effect in combination with the contact stress, particularly thermal stress local to the contact.

5. Author Statement

DIF – Conceptualisation, methodology, software, writing – original draft.

AW – Investigation, software, writing – review and editing.

JC – Resources, writing – review and editing.

Declaration of competing interest

The authors declare that they have no known competing financial interests or personal relationships that could have appeared to influence the work reported in this paper.

Data availability

Data will be made available on request.

Acknowledgements

The authors would like to acknowledge the Engineering and Physical Sciences Research Council through the Advanced Metallic Systems Centre for Doctoral Training (grant reference EP/L016273/1), and British Steel Ltd, for providing support for this research.

References

[1] Scott Cummings, Effectiveness of Corrective Grinding, TTCI Technology Digest, TD20-002, Associate of American Railroads, April 2020. https://aar.com/TD-eLibrary/details.php?ID=1020.

[2] UIC Leaflet 721, Recommendations for the Use of Rail Steel Grades, third ed., International union of railways, Union Internationale des Chemins de Fer, 16 rue Jean Rey F-75015, Paris, France, January 2015.

[3] Definitive guidelines on the use of different rail grades, Deliverable report D4.1.5GL Innotrack Project, Project TIP5-CT-2006-031415, available from: Chalmers University, Sweden, https://www.charmec.chalmers.se/innotrack/deliverables/sp4/d415-f3-railgrade_selection.pdf.

[4] Auckland metro RCF working group: Root cause assessment, KiwiRail and Auckland Transport, KiwiRail, Auckland, New Zealand, https://www.kiwirail.co.nz/assets/Uploads/documents/Auckland-RCF-Working-Group-Root-Cause-Assessment-Report-June-2021.pdf, June, 2021.

[5] R. Stock, D. Eadie, K. Oldknow, Rail grade selection and friction management: a combined approach for optimising rail–wheel contact, Ironmak. Steelmak. 40 (2) (2013) 108–114, https://doi.org/10.1179/1743281212Y.0000000038.

[6] C. Harwick, R. Lewis, R. Stock, The effects of friction management materials on rail with pre-existing RCF surface damage, Wear 384–385 (2017) 50–60, https://doi.org/10.1016/j.wear.2017.04.016.

[7] Network Rail Standard NR/L3/TRK/055, Work Instructions for Ultrasonic Rail Testing, Network Rail, One Eversholt Street, London, NW1 2DN.

[8] Z. Popović, V. Radović, L. Lazarević, V. Vukadinović, G. Tepić, Rail inspection of RCF defects, Metalurgija 52 (2013) 537–540, 4, https://hrcak.srce.hr/100836.
[9] Martin Hiensch, Michael Steenbergen, Rolling Contact Fatigue on premium rail grades Damage function development from field data, Wear 394–395 (2018) 187–194, https://doi.org/10.1016/j.wear.2017.10.018.
[10] D. Szablewski , S. Kalay, J. LoPresti, Development and Evaluation of high performance rail steels for Heavy Haul operations, International Heavy Haul Association Conference 2011 Special Technical Session, Calgary, Alberta, Canada.
[11] Y. Hu, L.C. Guo, M. Maiorino, J.P. Liu, H.H. Ding, R. Lewis, E. Meli, A. Rindi, Q. Y. Liu, W.J. Wang, Comparison of wear and rolling contact fatigue behaviours of bainitic and pearlitic rails under various rolling-sliding conditions, Wear (2020) 203455, https://doi.org/10.1016/j.wear.2020.203455. Volumes 460–461.
[12] M. Burstow, Experience of premium grade rail steels to resist rolling contact fatigue (RCF) on GB network, Ironmak. Steelmak. 40 (2) (2013) 103–107, https://doi.org/10.1179/1743281212Y.0000000042.
[13] H.M. El-sayed, M. Lotfy, H.N. El-din Zohny, H.S. Riad, Prediction of fatigue crack initiation life in railheads using finite element analysis, Ain Shams Eng. J. 9 (Issue 4) (2018) 2329–2342, https://doi.org/10.1016/j.asej.2017.06.003.
[14] J.W. Ringsberg, A. Bergkvist, On propagation of short rolling contact fatigue cracks, Fatig. Fract. Eng. Mater. Struct. 26 (2003) 969–983, https://doi.org/10.1046/j.1460-2695.2003.00657.x.
[15] W. Daves, M. Kráčalík, S. Scheriau, Analysis of crack growth under rolling-sliding contact, Int. J. Fatig. 121 (2019) 63–72, https://doi.org/10.1016/j.ijfatigue.2018.12.006.
[16] E. Magel, Rolling Contact Fatigue: A Comprehensive Review, U.S. Department of Transportation Report DOT/FRA/ORD-11/24, November 2011. https://railroads.dot.gov/sites/fra.dot.gov/files/fra_net/89/TR_Rolling_Contact_Fatigue_Comprehensive_Review_final.pdf.
[17] Roman Pohrt, Valentin L. Popov, Contact mechanics of rough Spheres: Crossover from fractal to Hertzian behavior, Advances in Tribology (2013), https://doi.org/10.1155/2013/974178. Article ID 974178, 4 pages, 2013.
[18] Gao Yan-Fei, A.F. Bower, Elastic–plastic contact of a rough surface with Weierstrass profile, Proc. R. Soc. A A. 462 (2006) 319–348, https://doi.org/10.1098/rspa.2005.1563.
[19] D. Nowell, D.A. Hills, Hertzian contact of ground surfaces, ASME. J. Tribol 111 (1) (January 1989) 175–179, https://doi.org/10.1115/1.3261869.
[20] D.P. Rooke, D.B. Rayaprolu, M.H. Aliabadi, Crack- line and edge Green's functions for stress intensity factors of inclined edge cracks, Fatigue Fracture Engng Mater. Structs 15 (1992) 441–461, https://doi.org/10.1111/j.1460-2695.1992.tb01286.x.
[21] D.I. Fletcher, A. Kapoor, Rapid method of stress intensity factor calculation for semi-elliptical surface breaking cracks under three-dimensional contact loading, Proceedings of the Institution of Mechanical Engineers, Part F: Journal of Rail and Rapid Transit. 220 (3) (2006) 219–234, https://doi.org/10.1243/2F09544097JRRT27.
[22] D.I. Fletcher, J.H. Beynon, A simple method of stress intensity factor calculation for inclined fluid-filled surface-breaking cracks under contact loading, Proc. Instn Mech. Engrs, PartJ: J. Engineering Tribology 213 (1999) 299–304, https://doi.org/10.1243/1350650991542839.
[23] D.I. Fletcher, J.H. Beynon, A simple method of stress intensity factor calculation for inclined surface breaking cracks with crack face friction under contact loading, Proc. Instn Mech. Engrs, Part J: J. Engineering Tribology. 213 (1999) 481–486, https://doi.org/10.1243/1350650991542839.
[24] H.K. Jun, D.H. Lee, D.S. Kim, Calculation of minimum crack size for growth under rolling contact between wheel and rail, Wear 344–345 (2015) 46–57, https://doi.org/10.1016/j.wear.2015.10.013.
[25] A. Kapoor, F. J Franklin, S. K Wong, M. Ishida, Surface roughness and plastic flow in rail wheel contact, Wear 253 (Issues 1–2) (2002) 257–264, https://doi.org/10.1016/S0043-1648(02)00111-4.
[26] A. Clarke, I.J.J. Weeks, R.W. Snidle, H.P. Evans, Running-in and micropitting behaviour of steel surfaces under mixed lubrication conditions, Tribol. Int. 101 (2016) 59–68, https://doi.org/10.1016/j.triboint.2016.03.007.
[27] P.-Z. Liu, W.-J. Zou, J. Peng, X.-D. Song, F.-R. Xiao, Study on the effect of grinding pressure on material removal behavior performed on a self-Designed passive grinding Simulator, Appl. Sci. 11 (9) (2021) 4128, https://doi.org/10.3390/app11094128.
[28] Jonas Lundmark, Rail Grinding and its Impact on the Wear of Wheels and Rails, Luleå University of Technology, Department of Engineering Sciences and Mathematics, Machine Elements, Licentiate thesis, 2007. http://urn.kb.se/resolve?urn=urn:nbn:se:ltu:diva-17238.
[29] Engineering Science Data Unit Item 85007, Contact Phenomena. III: Calculation of Individual Stress Components in Concentrated Elastic Contacts under Combined Normal and Tangential Loading, ESDU International, London, 1994.
[30] H.F. Bueckner, The Propagation of Cracks and the Energy of Elastic Deformation, 80E, Transactions of the American Society of Mechanical Engineers, 1958, pp. 1225–1230.
[31] D.I. Fletcher, P. Hyde, A. Kapoor, Modelling and full-scale trials to investigate fluid pressurisation of rolling contact fatigue cracks, Wear 265 (9–10) (2008) pp1317–1324, https://doi.org/10.1016/j.wear.2008.02.025.
[32] A. Wilby, J. Corteen, S. Lewis, R. Lewis, D.I. Fletcher, in: Efficient Laboratory Test Programme for Characterising Rail Steel Strain Accumulation, to Be Presented at 12th International Conference on Contact Mechanics and Wear of Rail/Wheel Systems (CM2022), Melbourne, Australia, September 2022, pp. 4–7.
[33] P.E. Bold, M.W. Brown, R.J. Allen, Shear mode crack growth and rolling contact fatigue, Wear 144 (1991) pp307–317, https://doi.org/10.1016/0043-1648(91)90022-M.
[34] S. Bogdanski, J. Stupnicki, M.W. Brown, D.F. Cannon, A two dimensional analysis of mixed-mode rolling contact fatigue crack growth in rails, in: Proceedings of the 5th International Conference on Biaxial/Multiaxial Fatigue and Fracture, vol. 2, Krakow, Poland, September 1997, pp. 189–206.
[35] BS EN ISO 4287, Geometrical Product Specification (GPS). Surface Texture: Profile Method. Terms, Definitions and Surface Texture Parameters, The British Standards Institution, 389 Chiswick High Road, London, W4 4AL, United Kingdom, 1998.